

See discussions, stats, and author profiles for this publication at: <https://www.researchgate.net/publication/26892390>

# Finding molecular dioxygen tunnels in homoprotocatechuate 2,3-dioxygenase: Implications for different reactivity of identical subunits

ARTICLE in BIOPHYSICS OF STRUCTURE AND MECHANISM · OCTOBER 2009

Impact Factor: 2.22 · DOI: 10.1007/s00249-009-0551-9 · Source: PubMed

CITATIONS

2

READS

22

## 3 AUTHORS:



Liang Xu

Dalian University of Technology

25 PUBLICATIONS 129 CITATIONS

SEE PROFILE



Weijie Zhao

Dalian University of Technology

26 PUBLICATIONS 44 CITATIONS

SEE PROFILE



Xicheng Wang

Dalian University of Technology

58 PUBLICATIONS 759 CITATIONS

SEE PROFILE

# Finding molecular dioxygen tunnels in homoprotocatechuate 2,3-dioxygenase: implications for different reactivity of identical subunits

Liang Xu · Weijie Zhao · Xicheng Wang

Received: 7 May 2009 / Revised: 9 September 2009 / Accepted: 24 September 2009 / Published online: 14 October 2009  
© European Biophysical Societies' Association 2009

**Abstract** Extradiol dioxygenases facilitate microbial aerobic degradation of catechol and its derivatives by activating molecular dioxygen and incorporating both oxygen atoms into their substrates. Experimental and theoretical studies have focused on the mechanism of the reaction at the active site. However, whether the catalytic rate is limited by O<sub>2</sub> access to the active site has not yet been explored. Here, we choose a recently solved X-ray structure of homoprotocatechuate 2,3-dioxygenase as a typical example to determine potential pathways for O<sub>2</sub> migration from the solvent into the enzyme center. On the basis of the trajectories of two 10-ns molecular dynamics simulations, implicit ligand sampling was used to calculate the 3D free energy map for O<sub>2</sub> inside the protein. The energetically optimal routes for O<sub>2</sub> diffusion were identified for each subunit of the homotetrameric protein structure. The O<sub>2</sub> tunnels formed because of thermal

fluctuations were also characterized by connecting elongated cavities inside the protein. By superimposing the favorable O<sub>2</sub> tunnels on to the free energy map, both energetically and geometrically preferred O<sub>2</sub> pathways were determined, as also were the amino acids that may be critical for O<sub>2</sub> passage along these paths. Our results demonstrate that identical subunits possess quite distinct O<sub>2</sub> tunnels. The order of O<sub>2</sub> affinity of these tunnels is generally consistent with the order of the catalytic rate of each subunit. As a consequence, the probability of finding the reaction product is highest in the subunit containing the highest O<sub>2</sub> affinity pathway.

**Keywords** Oxygen pathways · Oxygen tunnels · Extradiol dioxygenase · Implicit ligand sampling

## Introduction

Dioxygenases are non-heme iron-containing enzymes that play an important role in the biodegradation of catechol and its derivatives by catalyzing the cleavage of aromatic rings in either an intradiol or extradiol manner. Generally, the intradiol dioxygenases require Fe<sup>3+</sup> to cleave C–C bond between the phenolic hydroxy groups, producing *cis,cis*-muconic acid, whereas the extradiol dioxygenases use Fe<sup>2+</sup> or Co<sup>2+</sup> as a cofactor to cleave the C–C bond adjacent to the phenolic hydroxy groups, yielding 2-hydroxymuconaldehyde (Bugg and Lin 2001; Siegbahn and Haeffner 2004; Georgiev et al. 2008). As a result, an O<sub>2</sub> is activated and both oxygen atoms are inserted into the products. Several comprehensive reviews on dioxygenase mechanisms have been published recently, including those focusing on geometric and electronic structures (Wallar and Lipscomb 1996; Solomon et al. 2000), biomimetic modeling and intermediates (Costas et al.

**Electronic supplementary material** The online version of this article (doi:10.1007/s00249-009-0551-9) contains supplementary material, which is available to authorized users.

L. Xu · X. Wang (✉)  
Department of Engineering Mechanics, State Key Laboratory of Structural Analyses for Industrial Equipment,  
Dalian University of Technology, 116023 Dalian, China  
e-mail: guixum@dlut.edu.cn

L. Xu  
e-mail: xuliang0889@yahoo.com.cn

L. Xu  
Department of Chemistry, Dalian University of Technology,  
116023 Dalian, China

W. Zhao  
School of Chemical Engineering, State Key Laboratory of Fine Chemicals, Dalian University of Technology,  
116012 Dalian, China

2004; Kryatov and Rybak-Akimova 2005), and reaction mechanism (Abu-Omar et al. 2005; Bugg 2003; Lipscomb 2008). The catalytic mechanism of the non-heme iron catechol dioxygenase has also been theoretically studied by using density functional theory (Siegbahn and Haefner 2004; Deeth and Bugg 2003).

Many crystal structures of dioxygenases with or without bound substrates have been determined. From the sequence alignments of 35 extradiol dioxygenases it is apparent the three metal ligands His155, His214, and Glu267 (numbering from homoprotocatechuate 2,3-dioxygenase (2,3-HPCD); PDB entry 2IGA or 2IG9), a motif referred to as the 2-His-1-carboxylate facial triad, are strictly conserved residues in the active site pocket (Solomon et al. 2000). There are at least three possible mechanisms that could account for the dioxygen reactivity and the corresponding intermediates (Solomon et al. 2000). Recently, a crystal structure of  $\text{Fe}^{2+}$ -containing 2,3-HPCD (EC 1.13.11.15) from *Brevibacterium fuscum* has been resolved successfully, with three different intermediates in identical subunits of a single homotetrameric enzyme (Kovaleva and Lipscomb 2007). Thus, a general mechanism strategy for the diverse extradiol dioxygenases has emerged (Kovaleva and Lipscomb 2007; Kovaleva et al. 2007; Lipscomb 2008). Furthermore, these intermediates have not been observed independently in a crystal structure. How these subtle differences in identical subunits control the  $\text{O}_2$  binding, activation, and insertion still remains unclear. In addition, the crystallization was conducted in the slow substrate 4-nitrocatechol (4NC) in a low- $\text{O}_2$  atmosphere. Thus, the precise, atomic-resolution pathways for  $\text{O}_2$  migration in the protein, with predicted relative significant parts of the pathways, should help to rationalize the selectivity of the specific intermediate at the active site of each subunit and greatly facilitate the selection of specific site mutations for such studies.

In contrast with non-heme proteins,  $\text{O}_2$  migration pathways for myoglobin (Teeter 2004; Cohen et al. 2006; Cohen and Schulten 2007; Orłowski and Nowak 2007; Ruscio et al. 2008) and copper amine oxidase (Johnson et al. 2007), and  $\text{H}_2$  pathways for [Ni-Fe]-hydrogenase (Cohen et al. 2005; Leroux et al. 2008) and [FeFe]-hydrogenase (Teixeira et al. 2006) have been explored by experimental and computer simulations. To date, maps of  $\text{O}_2$  pathways in non-heme iron enzymes have only been characterized by molecular dynamics (MD) simulations for a small number of proteins, including quercetin 2,3-dioxygenase (van den Bosch et al. 2004; Fiorucci et al. 2006) and 12/15-lipoxygenase (Saam et al. 2007). The results from these studies have important implications for enzymatic activity and for protein engineering applications involving modifications of these pathways (Cohen and Schulten 2007). Previous studies have also consistently shown that gas pathways primarily originate

from localized thermal fluctuations of protein structure. Hence, these pathways are transient, and permanent gas tunnels cannot be detected in static crystal structures in most cases. It should be noted that migration pathways for small gas molecules inside proteins should be both geometrically and energetically favorable. Yet most previous studies have specifically focused on the energy aspect. A small body of work has investigated the dynamic cavities along the migration pathways (van den Bosch et al. 2004; Daigle et al. 2009).

In this study, we first report an all-atom MD simulation on the full length of solvated 2,3-HPCD complexed with 4NC as substrates. Then, the energetically favorable  $\text{O}_2$  channels in the four subunits are identified on the basis of implicit ligand sampling (Cohen et al. 2006, 2008). In combination with possible tunnels from cavities detected using CAVER software (Petřek et al. 2006; Damborský et al. 2007), we found four different  $\text{O}_2$  migration pathways for four identical subunits. Our results provide pertinent implications for the different catechol dioxygenase reactivity of a single homotetrameric enzyme.

## Materials and methods

### Force-field parameters for the active site residues

The starting coordinates for simulations were built from the 0.19 nm resolution refined X-ray crystal structure (PDB entry: 2IGA) (Berman et al. 2000; Kovaleva and Lipscomb 2007). This protein is a homotetrameric structure in which each subunit contains an active site. In particular, four subunits (A–D) were bound by product, alkylperoxo, superoxo, and alkylperoxo intermediates, respectively. The coordinate chosen for the  $\text{Fe}^{2+}$  site is the five-coordinate (Solomon et al. 2000, 2003) with the conserved 2-His-1-carboxylate motif (His155, His214, and Glu267) and one doubly deprotonated 4NC (Kovaleva and Lipscomb 2007) (Fig. 1). Following previous experiments and computational

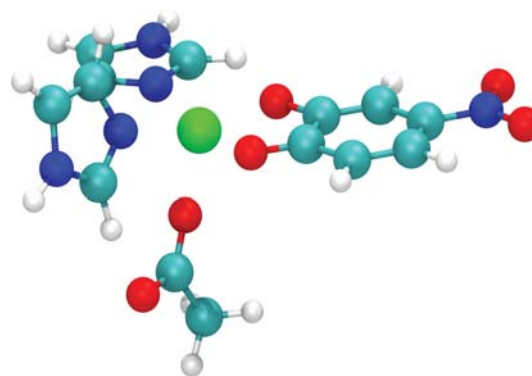


**Fig. 1** The model structure used to calculate force field parameters

work, the His, His, and Glu motif of the active site was modeled with two imidazoles and one acetate (Bugg 2003; Deeth and Bugg 2003; Costas et al. 2004), and their initial orientations were taken from the crystal structure. The initial orientation of 4NC was chosen as the result of superposition of 4NC with the three intermediates found in the crystal structure. The CHARMM force field parameter set of the model structure, and the partial atomic charges were calculated by using Paratool software, a plugin included with VMD software (Humphrey et al. 1996). Further computational details are given in the Supplementary Material. The resulting atomic charges are also given in Table S1 of the Supplementary Material.

### MD simulations

The substrates in four subunits of the crystal structure (PDB entry: 2IGA) were replaced by four 4NC dianions. Two methods, i.e., structure superimposition and Autodock 4.0 (Morris et al. 1998), were used to determine the binding mode of 4NC in each of the binding sites of the protein. It is noted that three Fe-bound ligands, (i.e., substrate 4NC, the alkylperoxo intermediate, and the ring-open product) can be well superposed (Kovaleva and Lipscomb 2007); therefore, the original orientation of the 4NC in each subunit adopted in the MD simulation could be the same for both methods.

Hydrogen atoms were added by using the PSFGEN plugin of VMD (Humphrey et al. 1996). All His residues were protonated at epsilon-N except His155 and His214 in each chain, because they were coordinated to the  $\text{Fe}^{2+}$  via epsilon-N.

All MD simulations were performed by use of the software package NAMD 2.6 (Phillips et al. 2005) with the CHARMM27 force field parameter set (MacKerell et al. 1998). The structure with 4NC bound in each subunit, together with crystal water molecules, was solvated to form a  $10 \times 11.8 \times 12.3$ -nm simulation water box by using the Solvate plugin of VMD. The resulting solvated system was neutralized by randomly adding  $\text{Na}^+$  ions in the bulk water by using the Autoionize plugin of VMD. The final system contains a total of 136,234 atoms, including the model protein, 37,825 water molecules and the added counterions.

First, the system was energy minimized for 10,000 steps, keeping protein, 4NC, and crystal water molecules fixed. Subsequently, the system was heated from 0 K to 300 K with heavy atoms restrained by using a spring with a variable constant from 20 kcal/mol/Å<sup>2</sup> to 10, 5, 2.5, 1.2, 0.6, and 0.1, with steps of 20 ps during first six stages and until 0 kcal/mol/Å<sup>2</sup>. Finally, the system was equilibrated for 100 ps and the simulation then lasted for another 20 ns at constant pressure and constant temperature (NPT). Langevin dynamics and the Langevin piston method were used to maintain the temperature at 300 K and the pressure

at 1 bar. Particle mesh Ewald (PME) was used for long-range electrostatics. The multiple time steps of 2, 2, and 4 fs were used for bonded, nonbonded, and long-range electrostatics interactions, respectively. Trajectory was saved every 1 ps, resulting in 20,000 frames from the 20-ns simulation. Then the whole trajectory was separated into two 10-ns trajectories and used in subsequent implicit ligand sampling and cavity identification.

### Implicit ligand sampling

The implicit ligand sampling method (Cohen et al. 2006, 2008) enables computation of 3D free energy or potential of mean force (PMF) map for a gas ligand at any location in a protein. As such, the interaction energy of a gas molecule with its surroundings is taken into account. This method has been implemented in VMD. Here, we apply this technique to our system. One  $\text{O}_2$  was placed in every trajectory frame on a finely-spaced 3D grid. Fifty conformations of  $\text{O}_2$  were sampled on each 0.1 nm<sup>3</sup> voxel. Recommended CHARMM parameters of  $\text{O}_2$  were used. Averaging over 10,000 frames from each of the 10-ns trajectories, the free energy at every grid position was obtained. Migration pathways of  $\text{O}_2$  could be constructed by connecting the energetically favorable areas of the maps.

### Identification of tunnels

The software CAVER (Petřek et al. 2006; Damborský et al. 2007) was applied to each of the 10-ns trajectories, determining hundreds to thousands of tunnels for each monomer of the protein. The energy profile along each tunnel was then constructed by superposing every tunnel profile on to the 3D free energy map generated using implicit ligand sampling. The most likely routes for  $\text{O}_2$  diffusion from the protein surface to the active site were thus identified by searching for the lowest-energy tunnels. Following this procedure for all detected tunnels allowed us to find the energetically preferred tunnel in the free energy map for each subunit. Residues lining the tunnels that could play key roles in controlling the passage of  $\text{O}_2$  were also extracted.

All calculations, including MD simulations were performed on the Lenovo clusters DeepComp 1,800 at the Department of Engineering Mechanics of Dalian University of Technology.

## Results and discussion

### Equilibrium properties of the system

It seems reasonable to replace the original Fe-bound ligand for a 4NC in each monomer of 2,3-HPCD simultaneously

as previous experimental studies have observed a similar phenomenon (Kita et al. 1999). Comparing the structure of the four subunits after minimization and equilibration (Fig. S2 in the Supplementary Material) provides direct evidence of a similar conformation. The non-bonded distances of interacting atoms at the active site of X-ray and MD-averaged structures are summarized in Table S2 of the Supplementary Material. As can be seen, the interactions of  $\text{Fe}^{2+}$  and His155, His214, Glu267, and 4NC calculated from the MD simulation are consistent with those observed in the X-ray structure (PDB entry 2IGA), indicating that the coordination environment of  $\text{Fe}^{2+}$  has not been perturbed during the 20-ns MD simulation (Table S2).

The structural stability of each monomer is evaluated on the basis of the root-mean-square deviation (RMSD) of each residue with regard to the crystal structure, as shown in Fig. 2. The modest deviations from the reference crystal structure suggest that each subunit is stable during the time-course of 20-ns MD simulation. However, the terminal residues of 350–364 fluctuate much within the second 10 ns. To compare the effect of structural difference on the  $\text{O}_2$  pathway, the whole trajectory was divided into two parts and analyzed separately.

#### $\text{O}_2$ migration pathways in four monomers

The implicit ligand PMF map for  $\text{O}_2$  inside 2,3-HPCD bound with 4NC is shown in Fig. 3. In water, the free energy is uniform (8.2 kJ/mol). All areas of the protein for which the PMF value is less than 8.2 kJ/mol are areas in

which it is more likely to find an  $\text{O}_2$  molecule than in water phase of identical volume. In each monomer we identify one major region that contains the most likely route for  $\text{O}_2$  diffusion from protein surface to the active center. The PMF map shows equally favorable  $\text{O}_2$ -accessible regions inside each monomer. The pathway for  $\text{O}_2$  movement with the lowest barrier starts at the free coordinate site (space left for  $\text{O}_2$ ) of Fe, close to both of the catecholate positions, and reaches to the protein–solvent boundary adjacent to Trp304, Tyr305, and Thr205 amino acids. Moreover, the regions with high probability of  $\text{O}_2$  occupation are quite wide. Although we cannot anticipate from the PMF map that  $\text{O}_2$  takes side-on binding rather than end-on orientation when coordinated to Fe (Kovaleva and Lipscomb 2007), the wide high-affinity area near the active site should favor formation of a side-on complex with iron. The C-terminal residues 323–362 were thought to form a “lid” over the substrate-binding pocket (Kovaleva and Lipscomb 2007). Here, Trp304, Tyr305, and Thr205 were found to line along the  $\text{O}_2$  pathway, suggesting that  $\text{O}_2$  could not share the same migration pathway with the substrate 4NC. For 12/15-lipoxygenase, copper amine oxidase, and cholesterol oxidase, previous studies have also suggested that dioxygen channels and substrate pathways are different (Saam et al. 2007). In contrast, the route for substrate entrance that also efficiently functions as  $\text{O}_2$  access pathway has been identified for cyclooxygenases (Saam et al. 2007).

It should be noted that the PMF values presented here are statistical averages sampled from 10,000 conformations. The pathways by which  $\text{O}_2$  enters the protein are

**Fig. 2** Root-mean-square deviations (RMSD) of each residue with regard to the X-ray structure in the first (black) and second (red) 10-ns MD simulations

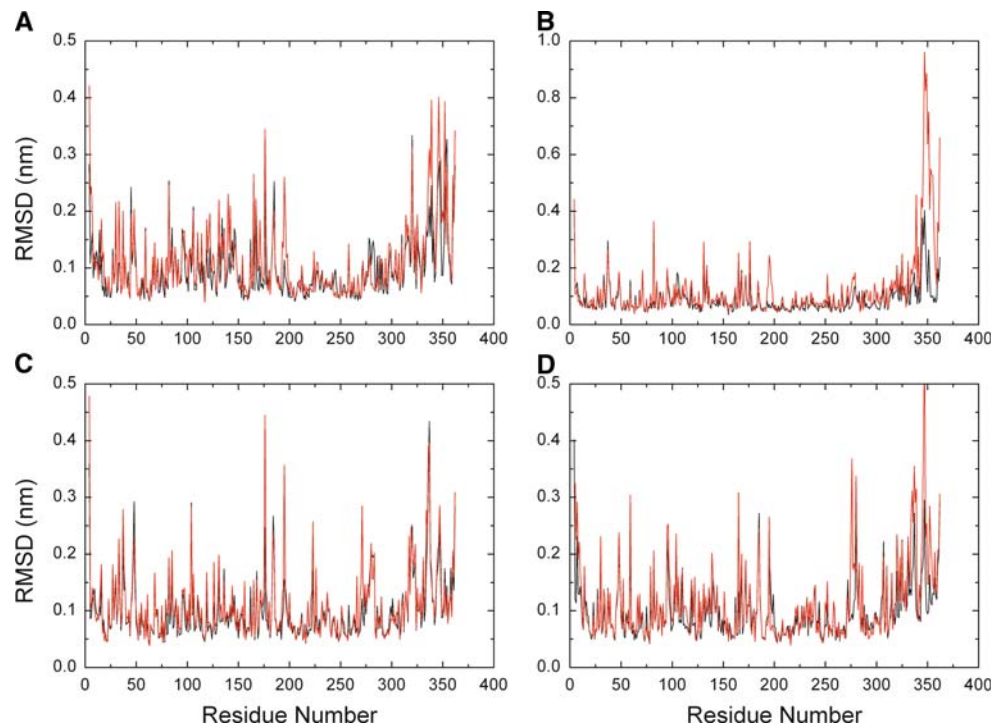
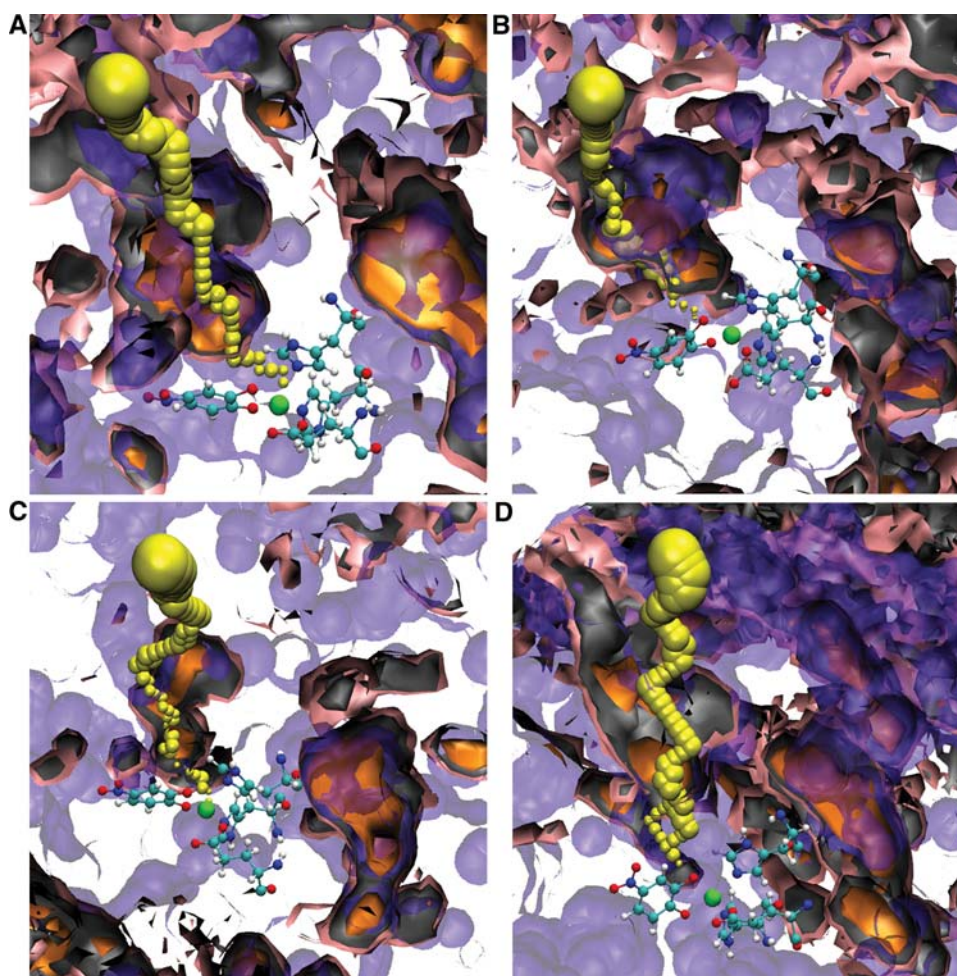




**Fig. 3** Implicit ligand PMF maps for  $O_2$  migration pathways inside the four subunits (A–D) of the protein, based on the first 10-ns MD simulation of the 2IGA PDB structure in the presence of one 4NC dianion in the active site of each subunit. Three free-energy isosurfaces with energy values of 0 kJ/mol (orange), 7.5 kJ/mol (gray), and 12.5 kJ/mol (pink) are superimposed. The Fe-bound ligands, i.e., His155, His214, Glu267, and the 4NC dianion are represented as a CPK model. The green ball represents the Fe atom. The static surface of each monomer is displayed as a transparent violet surf model. The yellow van der Waals spheres indicate the most favorable tunnels



assumed to result from diffusion through well-defined regions of the protein made possible by the protein's thermal fluctuation, rather than migration along permanent channels (Cohen et al. 2006; Cohen and Schulten 2007; Johnson et al. 2007; Saam et al. 2007). Therefore, the pathway identified by implicit ligand sampling resembles a chain of separate cavities that are transiently interconnected. In order to find subtle differences along  $O_2$  pathways in each monomer, cavities were characterized by use of CAVER software (Petřek et al. 2006; Damborský et al. 2007) based on two 10-ns MD simulations.

As suggested, cavities are short-lived and can hop inside the protein matrix, whereas elongated cavities that connect the active site to the solvent are rarely found. Such cavities, hereafter referred to as tunnels, are still geometrically favorable gas pathways. The lowest barrier tunnel profiles for each subunit, i.e., the tunnel radii and the energy values along the tunnels, are given in Figs. 4 and 5 (also see Figs. S3 and S4 for the second 10-ns result). The corresponding position of Fe was used as the starting point to calculate the distance but the first five points were not kept, because of the extremely large PMF values within such a narrow

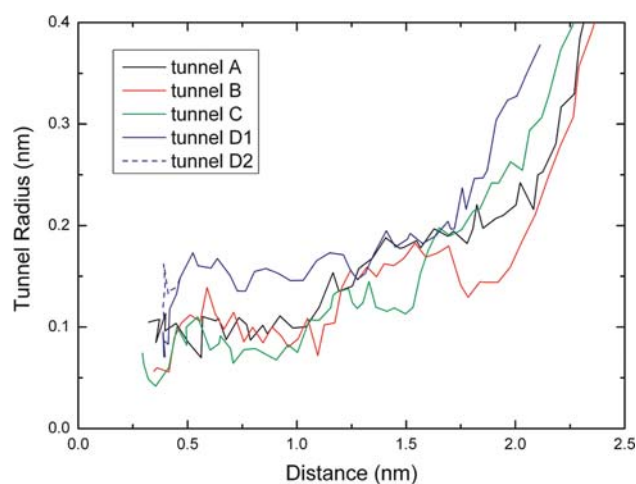


**Fig. 4** Optimal tunnel profiles for subunits A–D of 2,3-HPCD dioxygenase with 4NC, extending from the position of Fe to the bulk solvent. Only the result of the first 10-ns MD simulation is given. The result of the second 10-ns MD simulation is given in Fig. S3

region, as suggested by the CAVER software (Petřek et al. 2006; Damborský et al. 2007). The tunnel profiles (Figs. 4 and S3) clearly show that the tunnel in subunit D is

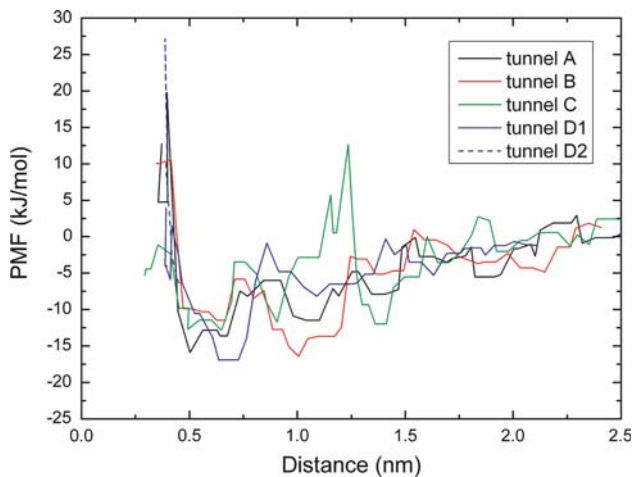


**Fig. 5** Energy profiles for  $O_2$  tunnels in subunit A–D, relative to the solvent (8.2 kJ/mol). Only the result of the first 10-ns MD simulation is given. The result of the second 10-ns MD simulation is given in Fig. S4

generally broader than the other three tunnels. Interestingly, tunnel D was observed to have two branches (tunnels D1 and D2) at the location close to the active center. On the other hand, the radii of the tunnel in subunit C are generally narrower, particularly in the position located approximately 1.25 nm from the iron. Another feature of the tunnel profiles is that there are two broader regions along the four tunnels. One lies at approximately 0.5 nm, in close proximity to the catalytic center Fe atom; another covers 1–1.3 nm. The latter wide area may serve as the anteroom to store  $O_2$ , because other studies have also indicated the presence of such region inside myoglobin (Cohen et al. 2006), copper-containing amine oxidase (Johnson et al. 2007), and 12/15-lipoxygenase (Saam et al. 2007). The interaction between  $O_2$  and other Fe-bound ligands reduces the tunnel radii approximately 0.3 nm from the origin (Fig. 4).

The energy profiles along these tunnels are somewhat surprising, as shown in Figs. 5 and S4. Two local minima of energy within 0.5–1.2 nm of the starting position were identified, corresponding to the broader region as mentioned earlier and as shown in Fig. 3. One minimum lies at approximately 0.5–0.7 nm for all of these tunnels, and another lies approximately 1.0–1.2 nm from the iron except for tunnel C. The unexpectedly high PMF values in this region of tunnel C suggest that the chance of finding  $O_2$  is far lower than in the same region in the other subunits; in particular, the probability of finding  $O_2$  in this region is much lower than in an equivalent volume of solvent, because the PMF values are above 0 kJ/mol. Recall the PMF map as shown in Fig. 3, the tunnels (represented as yellow van der Waals spheres) usually cross the low-energy isosurface, indicating these tunnels display

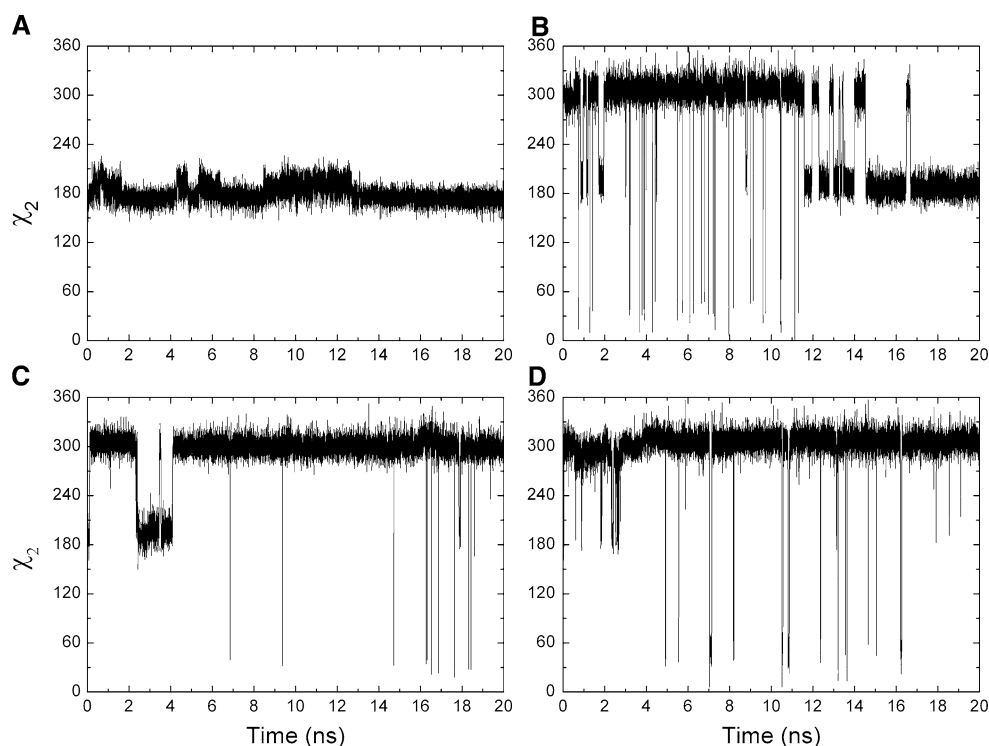
energetic preferences. Nevertheless, the central portion of the tunnel in subunit C apparently deviates from the low-energy area. This result also suggests that diffusion of oxygen is more difficult in subunit C than in other subunits.

In the case of tunnel A, it can be easily accessed by  $O_2$  because this route has the lowest energy barrier in the region close to the active center and moderately low energy barriers along this pathway. Although a local minimum is located at approximately 1.0 nm in tunnel B, it seems difficult for  $O_2$  to overcome the energy barrier and migrate into the active center. This energy-favorable basin may act as the anteroom for  $O_2$  diffusion. Tunnel D also possesses a wide energy-minimum region but much closer to the iron.  $O_2$  diffusion seems much easier in this tunnel, because the radii of cavities along this path are much larger than in the others (Fig. 4). However, once  $O_2$  migrates into the above basin, it can be easily trapped there, because of the high barrier around the basin. We also note that the bottleneck radii of one branch, i.e. tunnel D1, are much smaller than those of the other branch, tunnel D2 (Fig. 4), and the corresponding PMF values are much lower than for tunnel D2. As a consequence, tunnel D is characterized as a geometrically favorable but energetically unfavorable  $O_2$  diffusion pathway. However, after 10-ns structural relaxation, no branch is observed in tunnel D (Fig. S3). An additional feature of Fig. 5, e.g., at the beginning of pathway (<0.5 nm), is that the radii of the tunnel become so narrow that collision of  $O_2$  with the protein is more frequent and, consequently, the interaction energy is high. The energy profiles indicate that the  $O_2$  pathways in the same four subunit are characterized by different binding potential for  $O_2$  ( $A > B, D > C$ ) and relate well to the fact that the catalytic product is found in subunit A, the unstable alkylperoxo intermediate in subunits B and D, and the highly unstable superoxide intermediate in subunit C (Kovaleva and Lipscomb 2007).

Recent experimental studies have revealed that the diameter of the tunnel's bottleneck partially correlates with the observed rates of CO and  $H_2$  diffusion in hydrogenase (Leroux et al. 2008). In our analysis of the lowest-energy tunnels, the most important bottleneck radii approximately 0.38 nm from the iron are 0.11, 0.060, 0.042, and 0.095 nm for tunnels A, B, C and D, respectively. This radius at 0.38 nm was used, because it is common to all tunnels and located outside the volume occupied by the ligand (Daigle et al. 2009). Interestingly, this order is accord with the order of oxygen affinity of the four subunits. The bottleneck of each tunnel provides more evidence for the different rate of  $O_2$  transport in each subunit. As a result, the rate of catalytic reaction could be affected accordingly.

It has been realized that implicit ligand sampling can only describe the gas diffusion pathways defined by the protein's thermal motion. Slow conformational changes

**Fig. 6** Arg293 (R293)  $\chi_2$  as function of time for subunits A–D in the 20-ns MD simulation



such as the opening of a channel gate are beyond the simulation time scales (Cohen et al. 2008). The PMF map constructed from the current 10-ns MD simulation should be adequate to allow us to draw reliable conclusions, because the conformational changes among the four subunits are not significant in the first 10-ns MD simulation.

The electrostatic effect on the PMF map is omitted in this present study, as is usually done (Cohen et al. 2008). However, it may be of interest to investigate the electrostatic potential along these tunnels (Fig. S5 in Supplementary Material). Electrostatic analysis of the trajectory taken at 10 ns reveals the presence of positive electrostatic potential around the four tunnels that seems to affect  $O_2$  diffusion, binding, and activation. For example, the oxygen activation and insertion steps are sensitive to the protein environment, thus the positive electrostatic potential could stabilize the superoxo intermediate.

Inspecting the tunnel-surrounding residues, we find that the first local energy minimum located at 0.5–0.7 nm from the iron is formed by the residues bound to the iron, i.e., His155, His 214, Glu267, and the ligand 4NC. The second minimum centered at approximately 1.0 nm is between Arg293, His213, Trp304, Tyr305, and Thr205 just below the protein surface. However, the same region in tunnel C cannot be easily accessed by  $O_2$ , as mentioned above.

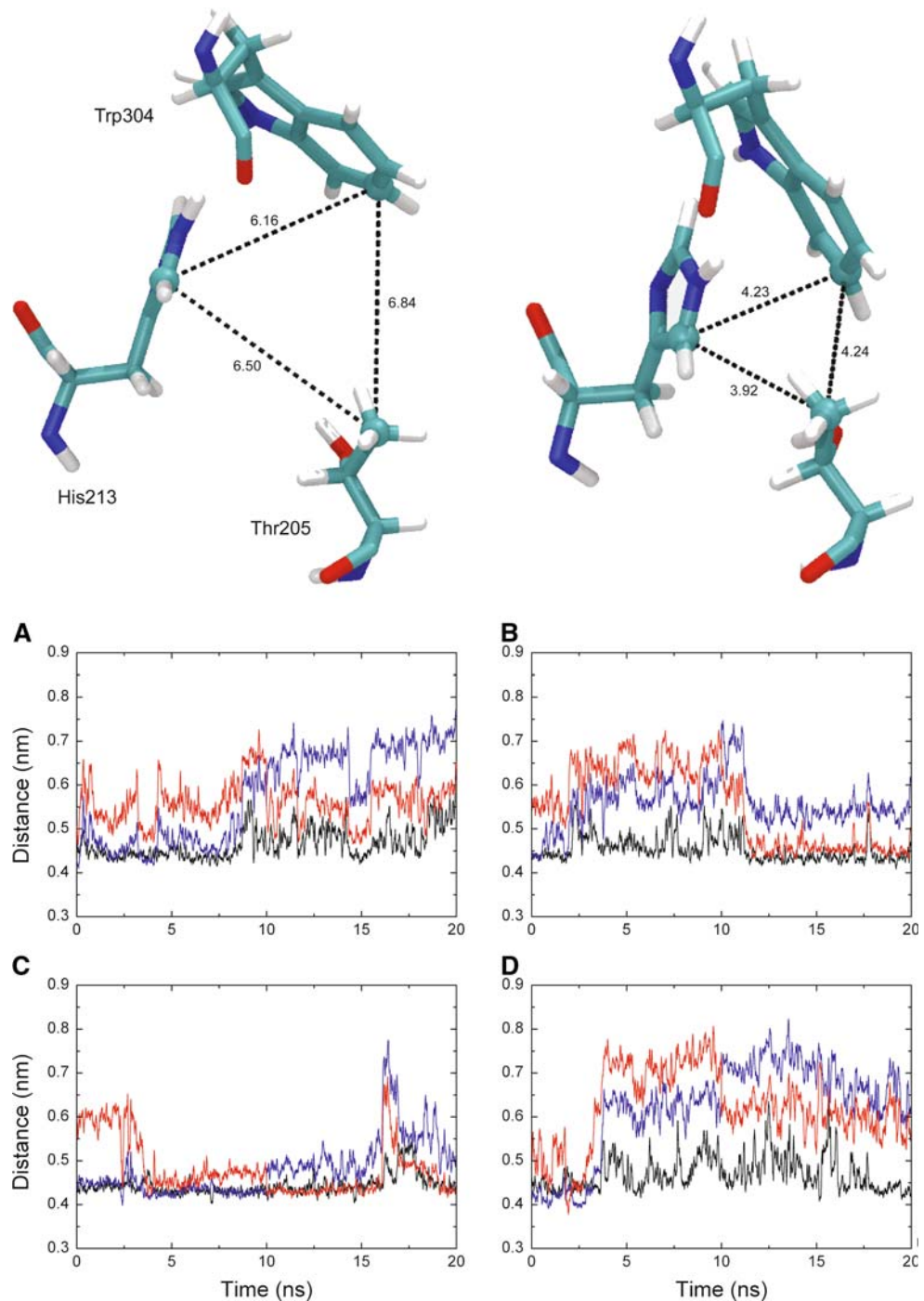
To assess the effect of side-chain flexibility of lining residues on tunnel formation, the  $\chi_1$  ( $N-C_\alpha-C_\beta-C_\gamma$ ) and  $\chi_2$  ( $C_\alpha-C_\beta-C_\gamma-C_{\delta 1}$ ) dihedral angles of these amino acids were

examined. It was found that except for Arg293, especially the  $\chi_2$  angle, the side-chain conformations of other amino acids are very similar (data not shown). The  $\chi_2$  angles of Arg293 were extracted from the 20-ns MD simulation and are plotted in Fig. 6. This shows that the side-chain of the Arg293 in subunit A is in the extended conformation ( $\chi_2 = -162.4^\circ$ ) for most of the time whereas in the other subunits Arg293 prefers to be in twisted conformation ( $\chi_2 = -42.1^\circ$ ). The collective movements of these amino acids were also examined by calculating the distance between different residues. It was found that the cavity composed by Thr205, His213, and Trp304 undergoes the so-called breathing motion (Tomita et al. 2009), as shown in Fig. 7. The expansion and contraction of the cavity may play specific role in controlling the passage of  $O_2$ . This result suggests that the increase of the distances between these residues concomitantly causes expansion of the cavity, leading to opening of the  $O_2$  pathway. It clearly shows that the frequency of the breathing motion of these residues in subunit C is far less than those in the other subunits, indicating the smallest chance of  $O_2$  access to the active site of subunit C.

With regard to the relevant residues lining the tunnels, as shown in Fig. 8,  $O_2$  might also interact with Asn157 and His213 when migrating to the iron in tunnel A. The additional interaction between  $O_2$  and the aromatic residue Trp192 in tunnel B could increase the energy barrier in the region adjacent to the binding site. Tunnel D is generally



**Fig. 7** *Top* snapshots of the expansion and contraction of the cavity (length in angstrom, Å). *Bottom*, distance between Thr205 C<sub>γ2</sub> and His213 C<sub>δ2</sub> (black), Thr205 C<sub>γ2</sub> and Trp304 C<sub>h2</sub> (red), His213 C<sub>δ2</sub> and Trp304 C<sub>h2</sub> (blue) observed in the 20-ns MD simulation



broad (Fig. 4) and the fluctuation of Arg293 (Fig. 6d) along with His213 could create an alternative O<sub>2</sub> diffusion pathway (tunnel D2) when approaching the active center.

It has been confirmed by experimental approaches that the rate of inhibition could be limited by CO or H<sub>2</sub> binding at the active sites in hydrogenase (Leroux et al. 2008). In particular, slowing of the transport of H<sub>2</sub>, D<sub>2</sub>, and HD in the channel reduces the probability that the intermediate produced, HD, exits the enzyme before it further reacts to

give H<sub>2</sub> (Leroux et al. 2008). This fact shows that the simultaneous presence of three different intermediates in a simple enzyme with four independent active sites could partially be attributed to the distinct O<sub>2</sub> pathways in 2,3-HPCD. Subunit A contains the most preferred O<sub>2</sub> pathway and, accordingly, the final product is found there. In the case of subunit C, the O<sub>2</sub> pathway is the least favorable and therefore, the highly unstable superoxo intermediate should be found with the highest probability. Subunits B and D

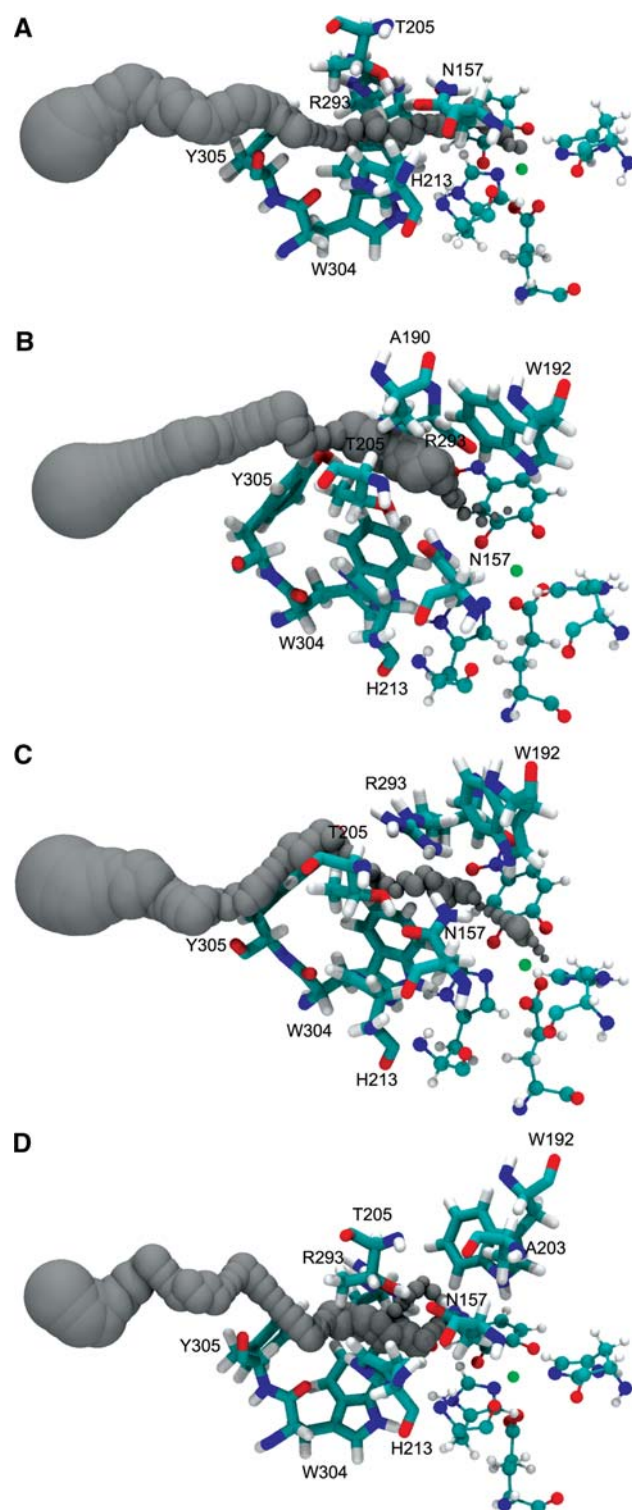


**Fig. 8** Snapshots of optimal routes for  $O_2$  movement in the four monomers (A–D). The relevant residues lining each tunnel are shown in licorice representation. The Fe-bound ligands are shown in CPK representation. The tunnels are represented as *gray solid surface*

contain different  $O_2$  tunnels and the alkylperoxo intermediate was found to be simultaneously present in them (Kovaleva and Lipscomb 2007). Moreover, it should be

noted that the rate of catalysis is not only limited by  $O_2$  access to the active site but also limited by its reaction at the active site (Leroux et al. 2008). In this way, characterization of  $O_2$  pathways alone could not be expected to explain all of the experimental outcomes. Recent experiments have shown that use of an alternative substrate, 4-sulfonylcatechol, and the Glu323Leu variant of HPCD, have led to formation of a new intermediate that seems to occur between the alkylperoxo intermediate and the product complexes in the reaction cycle (Kovaleva and Lipscomb 2008).

## Conclusions

To address the question of the different enzyme reactivity of each monomer in a homotetrameric 2,3-HPCD, implicit ligand sampling and tunnel detection were conducted on the trajectory of a 20-ns molecular dynamics simulation. Specific  $O_2$  migration tunnels that link the bulk solvent and the cavity of the enzyme have been probed. In contrast with randomized behavior,  $O_2$  diffusion in the four subunits is clearly limited to specific regions located within the conserved active site domain. A major finding of our study is that nominally identical subunits have distinct  $O_2$  affinity tunnels. In connection with recent experimental results for NiFe hydrogenase, the outcome of our computations suggests that the rate of dioxygenase-catalyzed reaction is generally correlated with the rate of access of  $O_2$  to the active center. The determination of the dynamic behavior of some key residues should aid understanding of the exquisite control over  $O_2$  binding for each subunit. To this end, this work described herein will be valuable for engineering non-heme iron dioxygenases to find intermediates by charactering  $O_2$  migration pathways.

**Acknowledgments** This work was supported by the Youth Foundation of DLUT (893103), National Natural Science Foundation (10772042), and the National Basic Research Program (2009CB918501) of China.

## References

- Abu-Omar MM, Loaiza A, Hontzas N (2005) Reaction mechanisms of mononuclear non-heme iron oxygenases. *Chem Rev* 105:2227–2252
- Berman HM, Westbrook J, Feng Z, Gilliland G, Bhat TN, Weissig H, Shindyalov IN, Bourne PE (2000) The protein data bank. *Nucleic Acids Res* 28:235–242
- Bugg TDH (2003) Dioxygenase enzymes: catalytic mechanisms and chemical models. *Tetrahedron* 59:7075–7101
- Bugg TDH, Lin G (2001) Solving the riddle of the intradiol and extradiol catechol dioxygenases: how do enzymes control hydroperoxide rearrangements? *Chem Commun* 941–952

- Cohen J, Schulten K (2007) O<sub>2</sub> migration pathways are not conserved across proteins of a similar fold. *Biophys J* 93:3591–3600
- Cohen J, Kim K, King P, Seibert M, Schulten K (2005) Finding gas diffusion pathways in proteins: application to O<sub>2</sub> and H<sub>2</sub> transport in Cpl [FeFe]-hydrogenase and the role of packing defects. *Structure* 13:1321–1329
- Cohen J, Arkhipov A, Braun R, Schulten K (2006) Imaging the migration pathways for O<sub>2</sub>, CO, NO, and Xe inside myoglobin. *Biophys J* 91:1844–1857
- Cohen J, Olsen KW, Schulten K (2008) Finding gas migration pathways in proteins using implicit ligand sampling. *Methods Enzymol* 437:439–457
- Costas M, Mehn MP, Jensen MP, Que LJr (2004) Dioxygen activation at mononuclear nonheme iron active sites: enzymes, models, and intermediates. *Chem Rev* 104:939–986
- Daigle R, Guertin M, Lagüe P (2009) Structural characterization of the tunnels of *Mycobacterium tuberculosis* truncated hemoglobin N from molecular dynamics simulations. *Proteins* 75:735–747
- Damborský J, Petřek M, Banáš P, Otyepka M (2007) Identification of tunnels in proteins, nucleic acids, inorganic materials and molecular ensembles. *Biotechnol J* 2:62–67
- Deeth RJ, Bugg TDH (2003) A density functional investigation of the extradiol cleavage mechanism in non-heme iron catechol dioxygenases. *J Biol Inorg Chem* 8:409–418
- Fiorucci S, Golebiowski J, Cabrol-Bass D, Antonczak S (2006) Molecular simulations reveal a new entry site in quercetin 2,3-dioxygenase. A pathway for dioxygen? *Proteins* 64:845–850
- Georgiev V, Borowski T, Blomberg MRA, Siegbahn PEM (2008) A comparison of the reaction mechanism of iron- and manganese-containing 2,3-HPCD: an important spin transition for manganese. *J Biol Inorg Chem* 13:929–940
- Humphrey W, Dalke A, Schulten K (1996) VMD—visual molecular dynamics. *J Mol Graph* 14:33–38
- Johnson BJ, Cohen J, Welford RW, Pearson AR, Schulten K, Klinman JP, Wilmot CM (2007) Exploring molecular oxygen pathways in *Hansenula polymorpha* copper-containing amine oxidase. *J Biol Chem* 282:17767–17776
- Kita A, Kita S, Fujisawa I, Inaka K, Ishida T, Horiike K, Nozaki M, Miki K (1999) An archetypical extradiol-cleaving catecholic dioxygenase: the crystal structure of catechol 2,3-dioxygenase (metapyrocatechase) from *Pseudomonas putida* mt-2. *Structure* 17:25–34
- Kovaleva EG, Lipscomb JD (2007) Crystal structures of Fe<sup>2+</sup> dioxygenase superoxo, alkylperoxo, and bound product intermediates. *Science* 316:453–457
- Kovaleva EG, Lipscomb JD (2008) Intermediate in the O–O bond cleavage reaction of an extradiol dioxygenase. *Biochemistry* 47:11168–11170
- Kovaleva EG, Neibergall MB, Chakrabarty S, Lipscomb JD (2007) Finding intermediates in the O<sub>2</sub> activation pathways of non-heme iron oxygenases. *Acc Chem Res* 40:475–483
- Kryatov SV, Rybak-Akimova EV (2005) Kinetics and mechanisms of formation and reactivity of non-heme iron oxygen intermediates. *Chem Rev* 105:2175–2226
- Leroux F, Dementin S, Burlat B, Cournac L, Volbeda A, Champ S, Martin L, Guigliarelli B, Bertrand P, Fontecilla-Camps J, Rousset M, Léger C (2008) Experimental approaches to kinetics of gas diffusion in hydrogenase. *Proc Natl Acad Sci USA* 105:11188–11193
- Lipscomb JD (2008) Mechanism of extradiol aromatic ring-cleaving dioxygenases. *Curr Opin Struct Biol* 18:644–649
- MacKerell AD, Bashford D, Bellott M, Dunbrack RL, Evanseck JD, Field MJ, Fischer S, Gao J, Guo H, Ha S, Joseph-McCarthy D, Kuchnir L, Kuczera K, Lau FTK, Mattos C, Michnick S, Ngo T, Nguyen DT, Prodhom B, Reiher WE, Roux B, Schlenkrich M, Smith JC, Stote R, Straub J, Watanabe M, Wiorkiewicz-Kuczera J, Yin D, Karplus M (1998) All-atom empirical potential for molecular modeling and dynamics studies of proteins. *J Phys Chem B* 102:3586–3616
- Morris GM, Goodsell DS, Halliday RS, Huey R, Hart WE, Belew RK, Olson AJ (1998) Automated docking using a Lamarckian genetic algorithm and empirical binding free energy function. *J Comput Chem* 19:1639–1662
- Orlowski S, Nowak W (2007) Oxygen diffusion in minihemoglobin from *Cerebratulus lacteus*: a locally enhanced sampling study. *Theor Chem Acc* 117:253–258
- Petřek M, Otyepka M, Banáš P, Košinová P, Koča J, Damborský J (2006) CAVER: a new tool to explore routes from protein clefts, pockets and cavities. *BMC Bioinformatics* 7:316
- Phillips JC, Braun R, Wang W, Gumbart J, Tajkhorshid E, Villa E, Chipot C, Skeel RD, Kale L, Schulten K (2005) Scalable molecular dynamics with NAMD. *J Comput Chem* 26:1781–1802
- Ruscio JZ, Kumar D, Shukla M, Prisant MG, Murali TM, Onufriev AV (2008) Atomic level computational identification of ligand migration pathways between solvent and binding site in myoglobin. *Proc Natl Acad Sci USA* 105:9204–9209
- Saam J, Ivanov I, Walther M, Holzthütter HG, Kuhn H (2007) Molecular dioxygen enters the active site of 12/15-lipoxygenase via dynamic oxygen access channels. *Proc Natl Acad Sci USA* 104:13319–13324
- Siegbahn PEM, Haefner F (2004) Mechanism for catechol ring-cleavage by non-heme iron extradiol dioxygenases. *J Am Chem Soc* 126:8919–8932
- Solomon EI, Brunold TC, Davis MI, Kemsley JN, Lee SK, Lehnert N, Neese F, Skulan AJ, Yang YS, Zhou J (2000) Geometric and electronic structure/function correlations in non-heme iron enzymes. *Chem Rev* 100:235–349
- Solomon EI, Decker A, Lehnert N (2003) Non-heme iron enzymes: contrasts to heme catalysis. *Proc Natl Acad Sci USA* 100:3589–3594
- Teeter MM (2004) Myoglobin cavities provide interior ligand pathway. *Protein Sci* 13:313–318
- Teixeira VH, Baptista AM, Soares CM (2006) Pathways of H<sub>2</sub> toward the active site of [NiFe]-hydrogenase. *Biophys J* 91:2035–2045
- Tomita A, Sato T, Ichiyanagi K, Nozawa S, Ichikawa H, Chollet M, Kawai F, Park SY, Tsuduki T, Yamato T, Koshihara SY, Adachi S (2009) Visualizing breathing motion of internal cavities in concert with ligand migration in myoglobin. *Proc Natl Acad Sci USA* 106:2612–2616
- van den Bosch M, Swart M, van Gunsteren WF, Canters GW (2004) Simulation of the substrate cavity dynamics of quercetinase. *J Mol Biol* 344:725–738
- Waller BJ, Lipscomb JD (1996) Dioxygen activation by enzymes containing binuclear non-heme iron clusters. *Chem Rev* 96:2625–2657